Measurement of the cross section for the $^{13}C(\alpha, n)^{16}O$ reaction and determination of the cross section for the $^{16}O(n, \alpha)^{13}C$ reaction

P. S. Prusachenko,* T. L. Bobrovsky, I. P. Bondarenko, M. V. Bokhovko, A. F. Gurbich, and V. V. Ketlerov
Institute for Physics and Power Engineering, Bondarenko square 1, Obninsk 249033, Russian Federation

(Received 26 August 2021; accepted 9 February 2022; published 18 February 2022)

The angular dependence of the differential cross sections for the $^{13}C(\alpha, n_0)^{16}O$ reaction was measured in the energy range 2.0–6.2 MeV using the time-of-flight method for separating neutrons corresponding to the ground state of the residual nucleus. The integrated total cross sections were derived from the measured data and the cross sections for the $^{16}O(n, \alpha_0)^{13}C$ reaction were determined using the reciprocity theorem. The cross sections obtained for the reaction $^{16}O(n, \alpha_0)^{13}C$ support the evaluation given in the ENDF/B-VIII.0 library.

DOI: 10.1103/PhysRevC.105.024612

I. INTRODUCTION

An accurate knowledge of the $^{16}O(n, \alpha)^{13}C$ reaction cross section is important for predicting the k_{eff} of nuclear reactors [1,2] and for assessing the accumulation of helium in reactor materials under irradiation with fast neutrons [3]. The importance of the inverse $^{13}C(\alpha, n)^{16}O$ reaction is due to the fact that it creates a background for measurements of geoneutrinos [4,5] and is a source of neutrons for the *s* process in nucleosynthesis [6]. The available experimental data obtained both for the direct [6–9] and the inverse reactions [4,6,10–13] are discrepant in the entire investigated range of neutron energies (2–10 MeV). Much effort has been made to reconcile the existing experimental data sets [2,14,15], create new evaluations of the cross sections [16–20], and conduct new experiments [5,20,21] to address this problem. However, at the moment there are still significant differences in the evaluated cross sections [19,20], and there is no understanding of the origin of the discrepancies in the experimental data of different authors. It was pointed out [2,3,14] that the problem cannot be solved without new experiments. The present work has been undertaken to meet this demand.

A detailed analysis of the available experimental information showed that the agreement between different data sets can be significantly improved by renormalization [2,14,15]. Thus the main problem to be addressed is reliable measurements of the absolute cross-section values. To that end it was decided to carry out measurements in such energy ranges of α particles where there were no narrow resonances and the cross section was relatively large. Based on these criteria, the measurements were performed in the following ranges of the α-particle energies: 2.0–2.4, 3.0–3.5, and 4.6–6.2 MeV. To reduce systematic errors, two experimental runs were carried out using different ^{13}C targets, with special attention paid to the experimental parameters that were critical for normalizing the data (neutron detection efficiency, number of projectiles hitting the target, target thickness), the determination of which was duplicated. In the first run, angular distributions of the differential cross sections for the $^{13}C(\alpha, n_0)^{16}O$ reaction were measured for 38 values of the α-particle energy using a target of amorphous carbon-13 deposited on a gold substrate 9 mm in diameter. In the second run, the excitation function of the $^{13}C(\alpha, n_0)^{16}O$ reaction at an angle of 0° was measured with the ^{13}C target (14 mm in diameter) deposited on a molybdenum substrate. In order to determine the cross sections for the inverse $^{16}O(n, \alpha)^{13}C$ reaction through the reciprocity theorem in all the energy ranges studied, a time-of-flight method was employed to separate neutrons corresponding to the ground state of the residual nucleus. The total cross sections were derived from the measured angular distributions of the differential cross sections by integration over the solid angle.

II. EXPERIMENTAL METHOD

A. Experimental setup

The schematic diagram of the experimental setup is shown in Fig. 1. The He++ pulsed beam with a repetition rate of 4 MHz from the IPPE 3-MV tandem accelerator was collimated by two apertures 5 and 6 mm in diameter located at the distance of 350 mm from each other. The energy calibration of the accelerator was made before the measurements using the method described in [22]. The ^{13}C target was tilted by 10° to the beam line in order to reduce neutron scattering in the target body at 90°. A silicon surface barrier detector (SBD) was located at an angle of 165° relative to the beam line at a distance of 185 mm from the target. It served as an independent monitor of the number of the particles hitting the target and the monitor of the carbon buildup on the target during the measurements. The target holder was used as a Faraday cup, the secondary electrons being suppressed by a guard electrode.

The neutrons emitted from the target were registered by a detector with a 40×40 mm *p*-terphenyl single crystal. The flight path between the target and the neutron detector

*Corresponding author: prusachenko.pavel@gmail.com

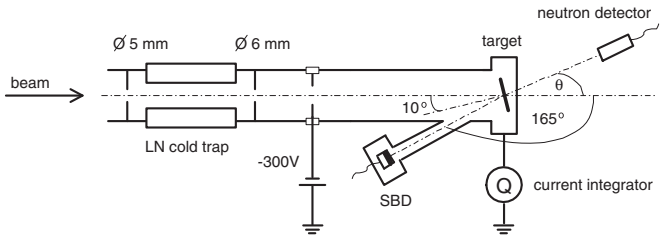

FIG. 1. The schematic diagram of the experimental setup (not to scale).

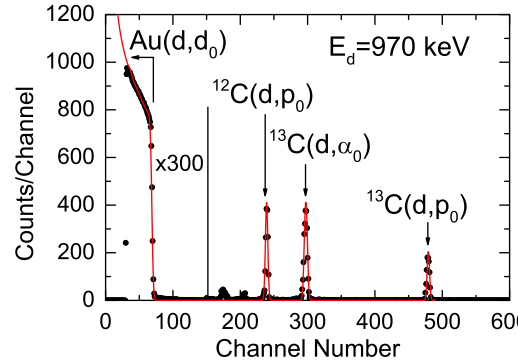

FIG. 2. The pulse-height spectrum of the charged particles detected at an angle of 150° for the ^{13}C target on a gold backing irradiated with deuterons. Dots: experimental values; line: simulation.

was measured using a FLUKE 424d laser rangefinder and amounted to 71.3 ± 0.4 cm for the first experimental run and to 65.2 ± 0.4 cm for the second one. The signals from the photomultiplier (PMT) anode were fed to the analog input of the wave-form digitizer (WFD) with a sampling rate of 500 MHz and the analog to digital converter resolution of 14 bits. The signals from the PMT last dynode served to trigger the digitizer. The signals from the pickup electrode of the accelerator chopper-buncher system were used as the start signals of the time-of-flight neutron spectrometer and were fed to the second analog input of the WFD. Both signals, from the PMT anode and from the pickup electrode, were simultaneously digitized and recorded in the list mode.

B. Target thickness measurement

The thickness of ^{13}C targets was determined by nuclear reaction analysis [23] through the $^{13}\mathrm{C}(d, p_0)^{14}\mathrm{C}$ ($Q = 5.952$ MeV) and $^{13}\mathrm{C}(d, \alpha_0)^{11}\mathrm{B}$ ($Q = 5.169$ MeV) reactions. The targets were placed in the scattering chamber at the center of the goniometer, perpendicularly to the beam axis and irradiated with a deuteron beam from the IPPE tandem accelerator. The beam was collimated to form a spot of 1 mm in diameter on the target. The reaction products were detected by the surface barrier detector located at 150° to the beam. The solid angle subtended by the detector was 1.02 msr. The deuteron beam energy was chosen to be 970 keV where the $^{13}\mathrm{C}(d, p_0)^{14}\mathrm{C}$ and $^{13}\mathrm{C}(d, \alpha_0)^{11}\mathrm{B}$ reaction cross sections were close to the maximum [24] and the cross section for the $^{12}\mathrm{C}(d, p_0)^{13}\mathrm{C}$ was well known. The reaction cross sections reported in [24] were verified at this energy by measurements with a thin natural carbon layer deposited on a gold foil, assuming a ^{13}C content of 1.1%. The cross sections for the $^{13}\mathrm{C}+d$ reactions were determined through the ratio of the areas of the corresponding peaks to the area of the $^{12}\mathrm{C}(d, p_0)^{13}\mathrm{C}$ reaction peak, the evaluated cross-section values for which was taken from SigmaCalc [25]. The results appeared to be in an agreement with the data given in [24] within the uncertainty (3.6%) reported in [24]. The cross sections [24] were then employed in the spectra simulation using the SIMNRA (version 7.03) program [26] by fitting the target thickness parameter until the theoretical values of the peak areas from the $^{13}\mathrm{C}(d, \alpha_0)^{11}\mathrm{B}$ and $^{13}\mathrm{C}(d, p_0)^{14}\mathrm{C}$ reactions were matched with the experimental ones. The Rutherford scattering of deuterons from the gold and molybdenum backings was used as an internal standard to double check the product of the solid angle by the number of projectiles incident on the target derived from the measured accumulated charge. The statistical error (1σ) was ≈2% for the peak corresponding to the $^{13}\mathrm{C}(d, \alpha_0)^{11}\mathrm{B}$ reaction, and ≈3% for the peak corresponding to the $^{13}\mathrm{C}(d, p_0)^{14}\mathrm{C}$ reaction. The number of ^{13}C nuclei per unit target area thus obtained appeared to be $(2.20 \pm 0.09) \times 10^{18}$ atoms $\times$cm^{-2} for the gold backing target and $(2.25 \pm 0.09) \times 10^{18}$ atoms $\times$cm^{-2} for the molybdenum backing target. The homogeneity of the targets was confirmed by measurements at five different points on each target. The concentration of the ^{12}C atoms derived from the $^{12}\mathrm{C}(d, p_0)^{14}\mathrm{C}$ reaction yield (see Fig. 2) was used to estimate the targets' enrichment with the ^{13}C isotope. The ^{13}C enrichment for the Au substrate target was found to be 94% and that for the target on Mo backing was 90%. The total target thickness in the energy units was approximately the same for both targets and ranging from 35 keV at 6.2 MeV to 72 keV at 2.0 MeV. A typical measured spectrum is shown in Fig. 2 along with the results of the simulation. The determination of the thickness of the targets was made twice—before the work and at the end. No deterioration of the targets was found.

C. Monitoring ^{12}C buildup and number of α particles impinged on the target

To monitor carbon buildup, backscattered α-particle spectra were periodically measured with SBD (see Fig. 3) at an energy of the incident α particles of 4280 keV. This energy corresponds to the right wing of a strong $^{12}\mathrm{C}(a, a)^{12}\mathrm{C}$ resonance located at 4.26 MeV and a very small cross section of elastic scattering of α particles from ^{13}C [27]. This made the $^{12}\mathrm{C}(a, a)^{12}\mathrm{C}$ peak clearly visible against the background of α particles backscattered from ^{13}C and the target substrate. The measured spectra for different time intervals elapsed since the start of the experiment and their simulation with SIMNRA are shown in Fig. 3. The obtained data on the thickness of deposited carbon (Fig. 4) were used to adjust the value of the energy of α particles reaching the target. It should be noted that, based on the ^{13}C content in the natural mixture of carbon isotopes, the amount of additional ^{13}C added to the target due to deposited carbon was insignificant (<0.5%).

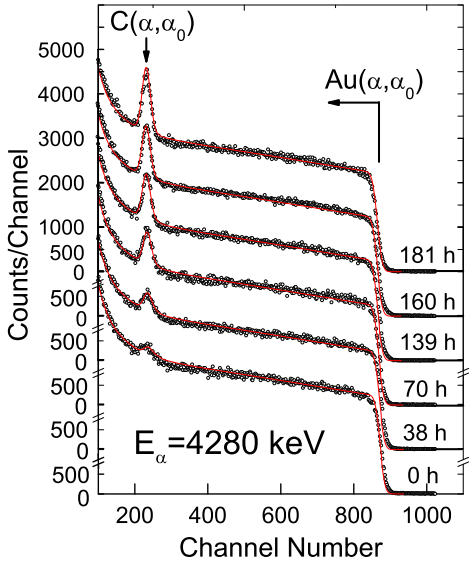

FIG. 3. Pulse-height spectra of α particles detected by SBD (dots) and results of the SIMNRA simulation (lines). The spectra are given for different time intervals elapsed since the start of the experiment.

The total charge of particles impinged on the target was measured using an Ortec 439 digital current integrator. The charge measurements were calibrated using a KEITHLEY 6220 precision current source, the output of which was connected to the target holder. The deviation between the current set at the source and the current measured by the integrator did not exceed 2% in the range 50–200 nA. This value was taken as an uncertainty in measuring the charge since the average beam current during measurements was ∼100 nA.

In order to double check the charge measurements, backscattered α-particle spectra were recorded using SBD followed by SIMNRA simulation. The number of particles impinged on the target was found through fitting to the height of the spectrum produced by the α particles backscattered from the target backing. Further processing of the time-of-flight spectra was carried out only under the condition that the measurement results of using the current integrator and SBD coincide within the uncertainty limits.

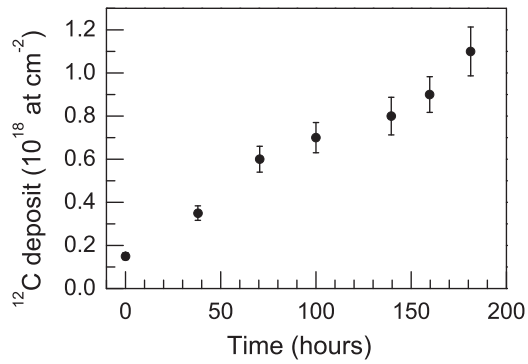

FIG. 4. Dependence of carbon deposits on the time elapsed since the beginning of the experiment.

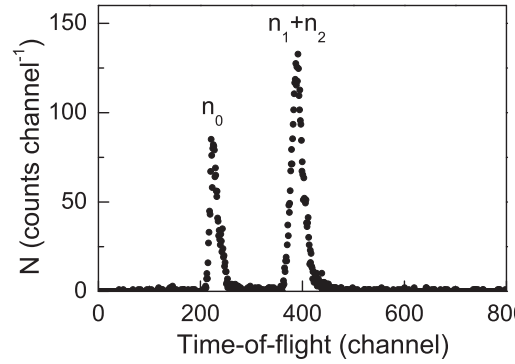

FIG. 5. Time-of-flight distribution of the neutron pulses, corresponding to the beam energy of 5910 keV and angle of 0°.

III. DATA ANALYSIS

A. Signal processing for the neutron spectrometer

At the first stage of signal processing, the time stamp positions for the start signal and the signal from the neutron detector were determined. For the start signals having a unified shape, the position of the cross-correlation function maximum was used as a time stamp. The pickup electrode signal, averaged over 2000 pulses and shifted to the zero position on the time scale, was used as a reference signal. In the case of the signal from the neutron detector, a software emulation of the constant fraction timing algorithm was used, similar to that described in [28], with the constant fraction value of 20%.

For the n/γ separation the correlation analysis of signals was used [29,30]. The signal from γ rays averaged over 5000 events in a narrow (850–900 keV electron equivalent) amplitude range was used as a reference signal for calculating the cross-correlation function. The value of the cross-correlation function maximum, normalized to the signal area calculated by numerical integration in a time window of 200 ns from the pulse start, was used as a separation parameter. The dynamic separation parameter threshold [30] was set to select events corresponding to neutrons.

A typical neutron time-of-flight spectrum thus obtained is shown in Fig. 5. The main factor influencing the timing resolution of the experiment was the width of the timing profile of the α-particle pulse, since the intrinsic timing resolution of the neutron detector used in the work was <0.5 ns. A typical α-particle pulse width, determined by full width at half maximum analysis of the prompt γ-ray peaks, was about 3–4 ns in the entire α-particle energy range. As can be seen from Fig. 5, the timing resolution of the experiment was sufficient to separate neutrons corresponding to the ground and the excited states of the residual nucleus, and to reject the spectrum part corresponding to neutron scattering in the walls.

B. Analysis of the neutron spectra

The differential cross section $d\sigma/d\Omega$ for the $^{13}C(\alpha, n_0)^{16}O$ reaction was determined according to the

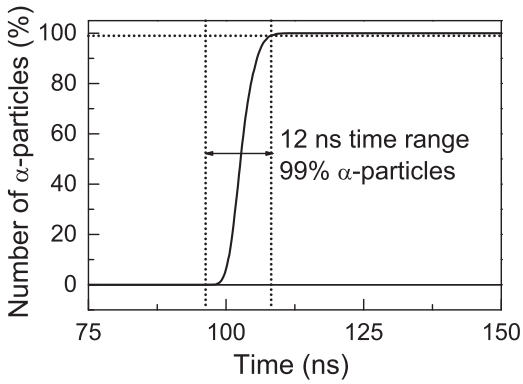

FIG. 6. Integral time distribution of α particles in a bunch. The distribution is given for the beam energy of 5884 keV.

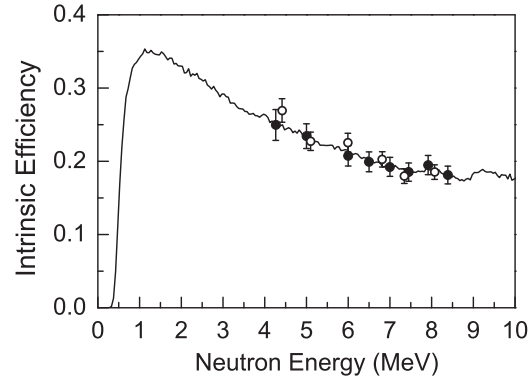

FIG. 7. The intrinsic efficiency of the neutron detector. Open dots: results obtained with a fission chamber as a neutron flux monitor; filled dots: results based on the measurements of the neutron time-of-flight spectra from the ^{2}H$(d,n)^3$He reaction; solid line: Monte Carlo calculations. The energy range of neutrons detected in the experiment was 3–9 MeV.

expression

$$\frac{d\sigma}{d\Omega}(\theta) = \frac{S_n(\theta)\gamma(\theta)}{N_\alpha \eta \varepsilon \Omega} 10^{24}\ \text{b}, \tag{1}$$

where S_n is the number of counts under the corresponding neutron peak in the time-of-flight spectrum for the angle θ after background subtraction; $\gamma(\theta)$ is the correction factor for the influence of multiply scattered neutrons; ε is the intrinsic efficiency of the neutron detector; N_α is the number of α particles incident on the target determined through the charge integration; η is the number of the ^{13}C atoms per unit target area in cm^2, Ω is the solid angle subtended by the neutron detector.

The solid angle was determined based on the geometrical parameters of the detection system (the flight path and the neutron detector diameter). The neutron peak area was determined by channel-by-channel summation within the time window corresponding to the beam pulse duration. The duration of the pulse was preliminarily estimated for each value of the α-particle energy using SBD. The fast signal from SBD was digitized and the pulse amplitude and time stamp were determined for each digitized signal. Then, signals were selected from the narrow amplitude window near the maximum energy of α particles scattered on the target backing. An example of the integral time distribution for the α particle pulse is shown in Fig. 6. For most of the energy values, 99% of the α particles fell within the time range ($t_{0.99}$) 10–20 ns after the pulse start. The integration time range of the neutron peaks was chosen to be larger than this value ($1.2t_{0.99}$) to take into account the possible difference in the time characteristics of the two detectors. To determine the background, ten points were selected to the right and left of the neutron peak integration limits followed by linear interpolation.

C. Neutron detector efficiency

The intrinsic efficiency of the neutron detector was obtained by Monte Carlo calculations using the GEANT4 framework [31,32]. The simulation was carried out using the G4NDL-4.6 library in combination with the NRESP71 model to simulate reactions on carbon [33]. The simulation results are shown in Fig. 7. The uncertainty of the simulation results, with the uncertainty of the detector geometric parameters and the uncertainty in determining the neutron detection threshold being taken into account, was ≈3% for the neutron energies of interest (3–9 MeV).

The simulation results were experimentally verified using two different methods, in which the ^{2}H$(d,n)^3$He reaction was used as a neutron source. In the first case, the measurement of the intrinsic detection efficiency of the neutron detector was performed using a fission chamber with four identical double-sided $^{235}U_3O_8$ (Ø30 mm of the active area) layers for monitoring the neutron flux. The number of ^{235}U atoms in each layer was found using an HPGe detector based gamma spectrometer. The spectrometer efficiency was determined using γ sources, the activity of which was known with an accuracy of 2%. A correction for different diameters of uranium layers and γ sources was performed by means of the simulation using GEANT4. The ^{235}U γ rays with the energy of 143.7, 163.3, and 185.7 keV were used for the analysis, the branching ratio for the γ lines being taken from the ENDF-B/VIII.0 library [19]. The detection efficiency for the fission fragments in the chamber was determined in a separate experiment by the method proposed in [34] and was found to be 91 ± 3% in a good agreement with the simulated fission fragments registration efficiency (92 ± 1%). The monitor detector and the investigated one were located at angles of ±20° relative to the beam line inside shielding collimators. The quasimonoenergetic neutrons were generated by the gaseous deuterium target with a gas cell length of 20 mm and the deuterium pressure of 2 atm irradiated by the pulsed deuteron beam. The total systematic measurement uncertainty in this case was the sum of the uncertainty in the total number of ^{235}U atoms in the layers (∼3%), the uncertainty in the detection efficiency of fission fragments (∼3%), and the uncertainties in the distance from the target to the corresponding detector (∼2%).

In addition, the detection efficiency of the neutron detector was found by measuring the neutron time-of-flight spectra from the ^{2}H$(d,n)^3$He reaction, the total and differential cross sections for which are well known [35–37]. The target used was a thin layer of deuterium-saturated titanium deposited on

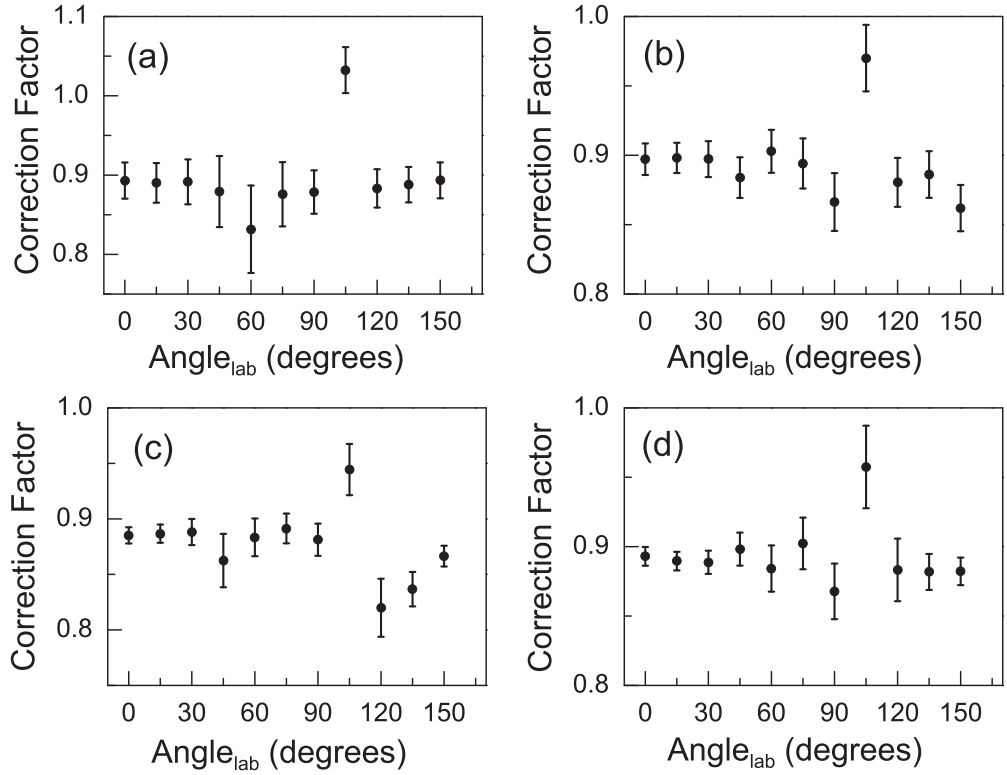

FIG. 8. Correction factor for multiple neutron scattering for selected α-particle energies. (a) α-particle energy of 2219 keV, (b) 3389 keV, (c) 4709 keV, (d) 5180 keV.

the molybdenum backing. The number of deuterium atoms in the target was determined by nuclear reaction analysis through the ^{2}H$(d, p)^3$H reaction, as described in [28], and appeared to be equal to $(1.30 \pm 0.07) \times 10^{19}$ atoms $\times$ cm^{-2}. The neutron detector was placed in the central channel of the massive shielding collimator at an angle of 0° relative to the beam line. When calculating the uncertainties of the efficiency measured by this method, the uncertainty of the number of deuterium atoms in the target (≈5%), the uncertainty of the differential cross sections for the ^{2}H$(d, p)^3$H reaction (≈4% according to the data of [35]), the uncertainty in measuring the beam current (2%), the solid angle uncertainty (1%), and statistical uncertainty (1σ, 1–3% depending on the neutron energy) were taken into account. The results of measuring the efficiency by both methods are shown in Fig. 7 in comparison with the simulated curve. Additional simulation aiming to estimate the influence of multiple scattered neutrons on the results of the efficiency measurement showed that their contribution to the measured spectra was less than 2% for the measurement geometry used. The simulation results and the results of the two experiments were in good agreement with each other within 4%. Hence, to calculate the differential cross section by the formula (1), the simulated efficiency curve with an assigned uncertainty of 4% was used.

D. Correction for multiple neutron scattering

The background from neutrons scattered in the walls of the experimental hall was well separated from neutrons corresponding to the ^{13}C$(\alpha, n_0)^{16}$O reaction by time of flight. However, the events caused by neutrons scattered on the detector package and its mounting elements may fall within the integration range of the neutron peak. The contribution of these events was calculated by the Monte Carlo method in the GEANT4 environment. For this, the geometry of the experiment was simulated in detail, including the materials surrounding the detector and the target holder of the accelerator. For each value of the α-particle energy and the position of the detector relative to the beam line, the calculation was carried out twice with the same number of primary particles—taking into account all the materials that make up the experimental setup (option a), and when all materials were removed except for the detector material (option b). The correction factor was calculated as the area ratio of the two neutron distributions, obtained for option a and option b, summed up within the integration limits of the experimental neutron peak for the current energy and angle values. The simulated correction factors for several values of the α-particle energies are shown in Fig. 8. As can be seen from the figure, the correction factor has a weak dependence on the angle except for 105°, where neutrons have to pass a long way through the target holder flange material on their path to the detector. When estimating the uncertainty of the obtained factor, the uncertainty associated with the differences in the cross sections in different nuclear data libraries was taken into account in addition to the statistical error (1σ). For this purpose, a number of additional calculations were performed for several values of the α-particle energy using different nuclear data libraries (ENDF/B-VIII.0, JENDL-4.0u). The maximum variation in the obtained

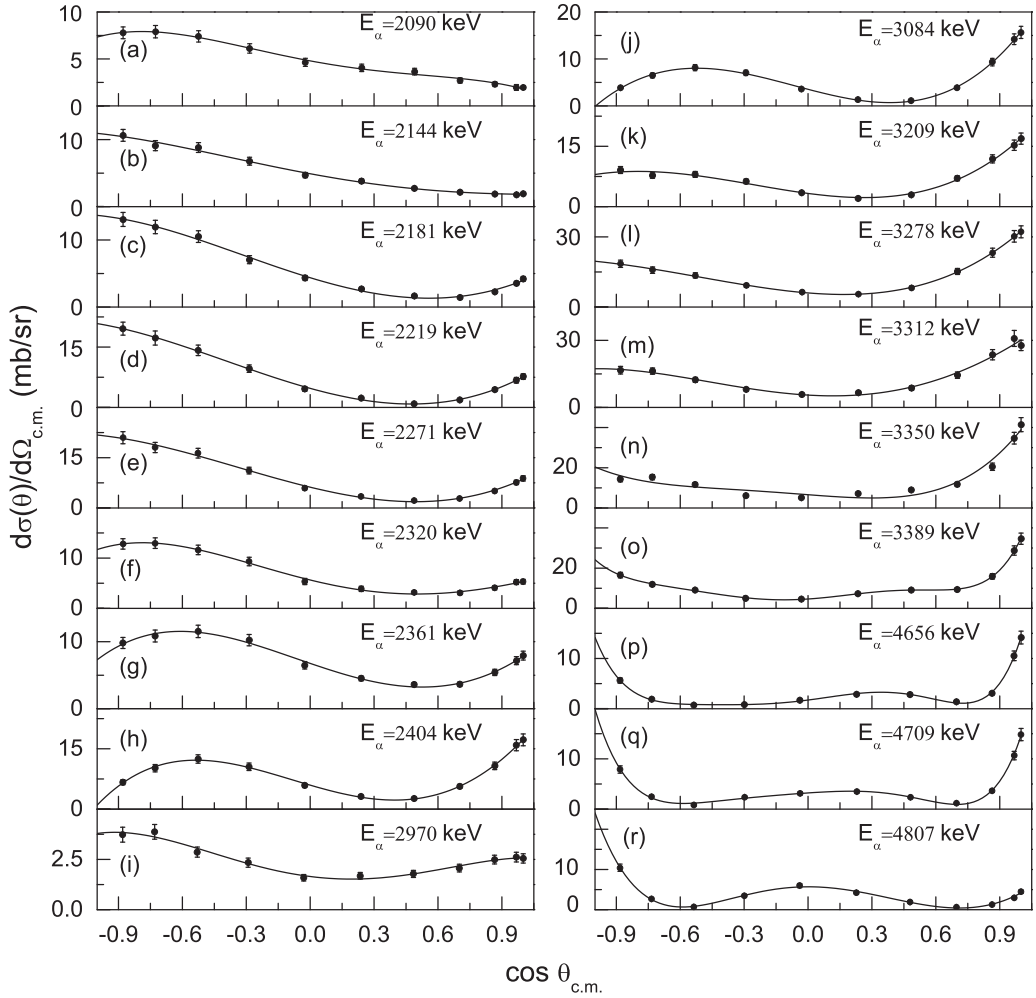

FIG. 9. The angular distributions for the $^{13}C(\alpha, n_0)^{16}O$ reaction in the α-particle energy range 2090–4807 keV. Dots: experimental data; solid lines: approximation by Legendre polynomials.

correction factors did not exceed 2% and this value was taken as an uncertainty.

IV. RESULTS AND DISCUSSION

The acquired angular distributions (see the Supplemental Material [38]) for the $^{13}C(\alpha, n_0)^{16}O$ reaction are shown in Figs. 9 and 10. Each angular distribution was approximated by Legendre polynomials followed by integration over the entire solid angle to obtain a total reaction cross section. The statistical uncertainty for total cross sections was in the range 0.5–1.5%. The systematic uncertainty budget is presented in Table I. The α-particle energies were calculated at the center of the target taking into account carbon deposits. The thickness of the ^{13}C layer was the main factor affecting the energy resolution of the measured cross-section values, while the effect of the beam energy ripple (<0.1%) was negligible. The energy resolution determined from full energy losses of α particles in target in this experiment is in the range 70–36 keV depending on the beam energy. The cross section for the inverse $^{16}O(n, \alpha_0)^{13}C$ reaction was derived by applying the reciprocity theorem.

The differential cross sections for the $^{13}C(\alpha, n_0)^{16}O$ reaction measured at an angle of 0° in two experimental runs together with data from the literature [12,27,39] are shown in Fig. 11. As can be seen from the figure, all the results except for [12] are in a good agreement and the data of [12] should be multiplied by a factor of 2.25 in order to harmonize them with [27] and the present measurements.

The cross sections obtained in this work (see the Supplemental Material [38]) were compared with the evaluations given in the ENDF-B/VIII.0 [19] and JENDL-4.0/HE [20] libraries, as well as with the experimental data of other

TABLE I. Systematic uncertainty budget.

Uncertainty source	Contribution, %
Target thickness	4
Detector efficiency	4
Beam current	2
Solid angle	2.5
Multiple scattering	2
Total	6.8

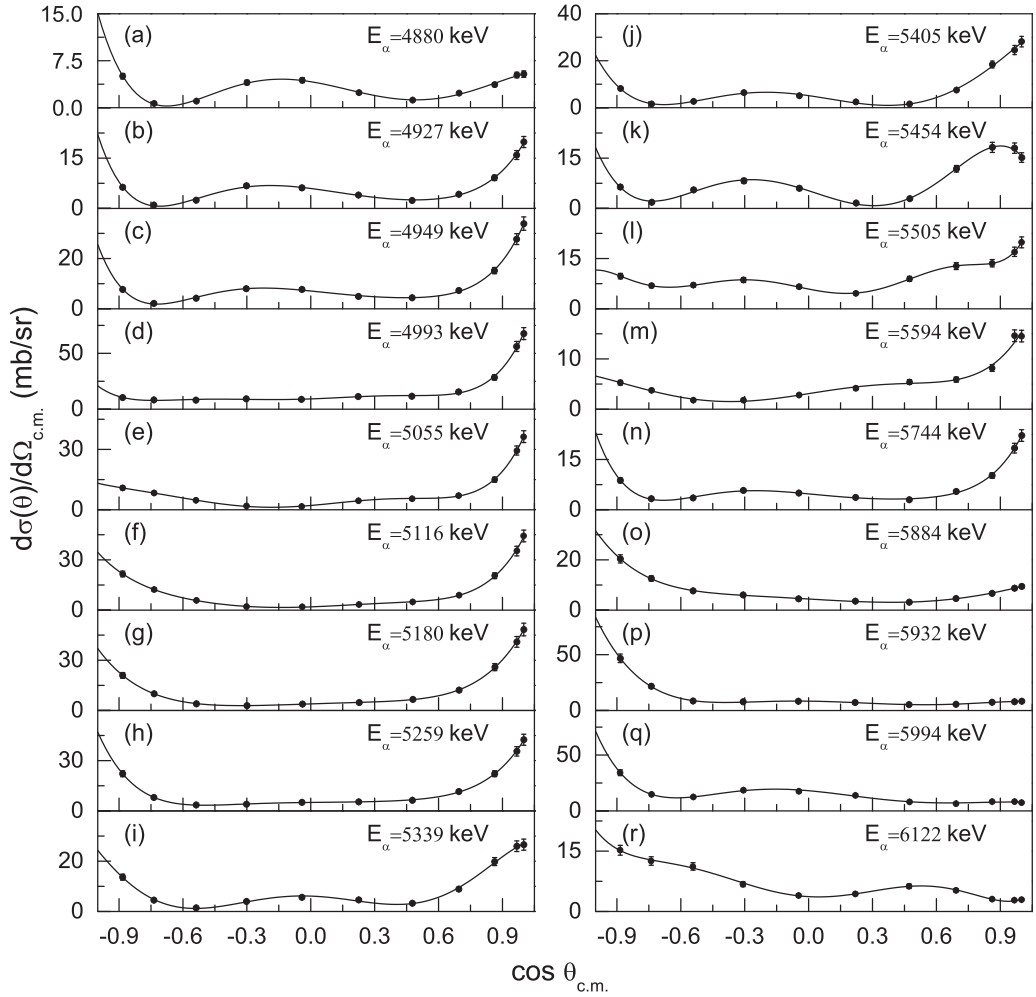

FIG. 10. The same as in Fig. 9 but for the α-particle energy range 4880–6122 keV.

authors (Figs. 12 and 13). The comparison took into account the energy resolution indicated in the published works. The present data are conforming with the evaluation given in the ENDF-B/VIII.0 library for the ^{16}O$(n,\alpha_0)^{13}$C reaction cross section over the entire range of neutron energies. The results published by Khryachkov *et al.* [8] are consistent with the data obtained in the present work only for neutron energies above 6 MeV. The rest of the experimental data [4,6–13], obtained

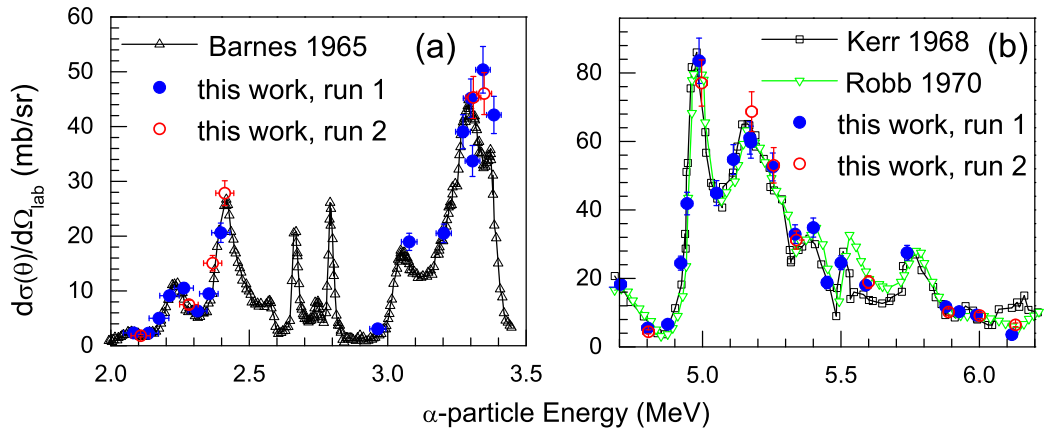

FIG. 11. The comparison of the differential cross sections for the ^{13}C$(\alpha,n_0)^{16}$O reaction measured at an angle of 0° in two experimental runs with data from the literature for 2.0–3.5 MeV [39] (a) and 4.75–6.20 MeV [12,27] (b). The Robb data were multiplied by a factor of 2.25.

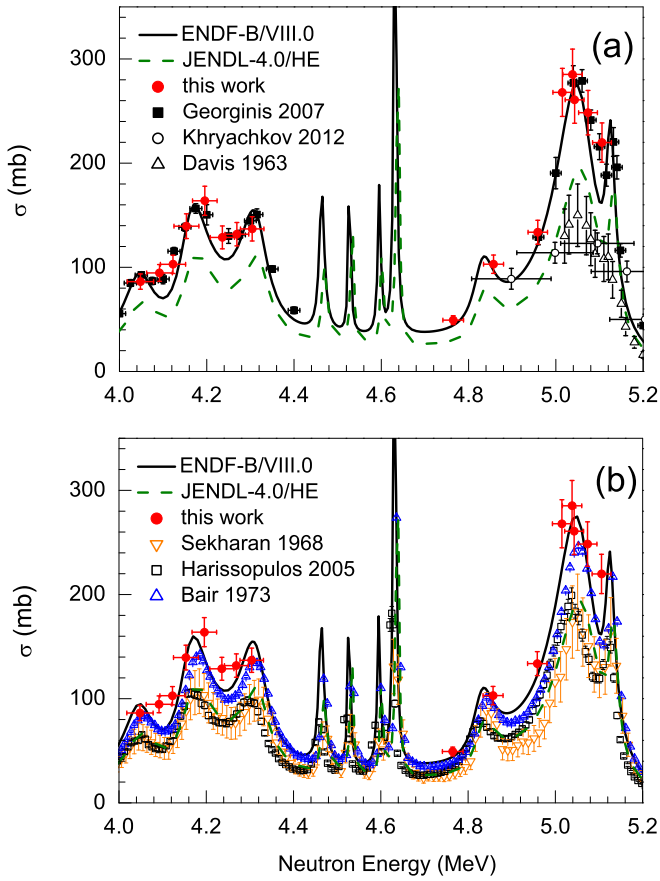

FIG. 12. The ^{16}O$(n,\alpha_0)^{13}$C reaction cross section in the neutron energy range 4.0–5.2 MeV, obtained via direct (a) and inverse (b) reactions, in comparison with the ENDF/B-VIII.0 and JENDL-4.0/HE evaluations, and other experimental data [4,7–9,11,13]. The data by Bair are given with the normalization recommended by the authors.

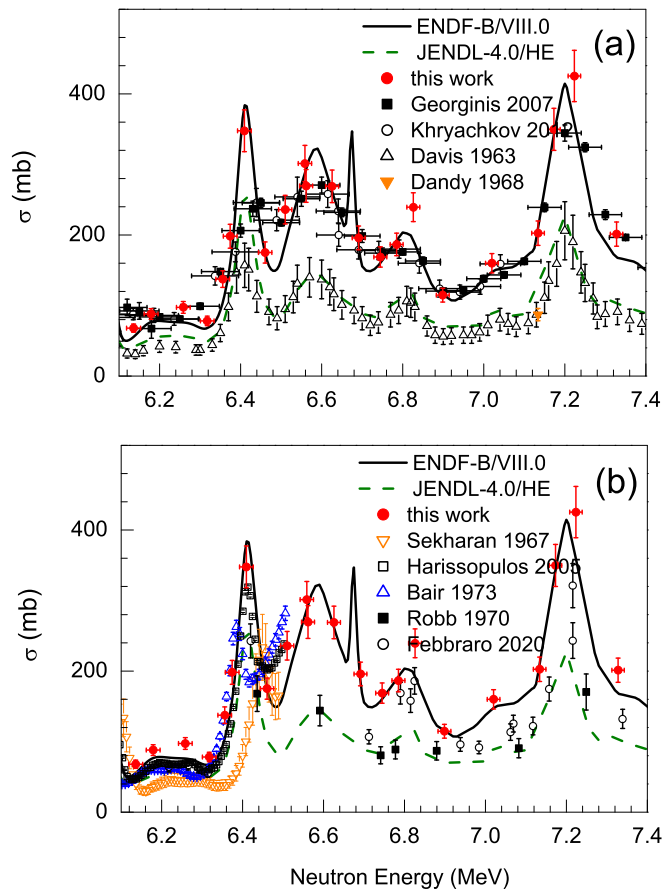

FIG. 13. The same as in Fig. 12 but for the neutron energy range 6.0–7.5 MeV. The experimental data are from Refs. [4,5,7–13].

both in the direct and inverse reaction measurements, differ significantly from the present data and from each other. The data by Davis *et al.* [9] and Sekharan *et al.* [11] are presented with large uncertainties (∼20%), which makes comparison with them problematic.

V. CONCLUSIONS

The differential and integral cross sections for the ^{13}C$(\alpha,n_0)^{16}$O reaction were acquired for the energy range 2.0–6.2 MeV. The time-of-flight method in combination with the digital signal processing was used for suppressing the contribution of the neutrons from the first exited level of the residual nucleus. In order to minimize systematic errors the determination of the experimental parameters critical for normalizing the data was duplicated. The ^{16}O$(n,\alpha_0)^{13}$C reaction cross section was calculated using the reciprocity theorem. The obtained results support the ENDF-B/VIII.0 evaluation.

ACKNOWLEDGMENTS

The authors are grateful to Dr. M. Kokkoris for providing one of the ^{13}C targets used in the work and to Dr. V. Khryachkov for valuable comments.

[1] M. B. Chadwick *et al.* (CIELO Collaboration), The CIELO Collaboration: Neutron reactions on ^{1}H, ^{16}O, ^{56}Fe, ^{235,238}U, and ^{239}Pu, Nucl. Data Sheets **118**, 1 (2014).

[2] M. B. Chadwick *et al.* (CIELO Collaboration), CIELO Collaboration Summary Results: International evaluations of neutron reactions on uranium, plutonium, iron, oxygen and hydrogen, Nucl. Data Sheets **148**, 189 (2018).

[3] A. Courcelle, Need for $^{16}O(n,\alpha)$ measurement and evaluation in the range 2.5 to 10 MeV, technical report, CEA Cadarache (2005), https://www.oecd-nea.org/dbdata/hprl/tmp/Need for O16(n,alpha).pdf.

[4] S. Harissopulos, H. W. Becker, J. W. Hammer, A. Lagoyannis, C. Rolfs, and F. Strieder, Cross section of the ^{13}C$(\alpha,n)^{16}$O reaction: A background for the measurement of geo-neutrinos, Phys. Rev. C **72**, 062801 (2005).

[5] M. Febbraro, R. J. deBoer, S. D. Pain, R. Toomey, F. D. Becchetti, A. Boeltzig, Y. Chen, K. A. Chipps, M. Couder, K. L. Jones *et al.*, New ^{13}C$(\alpha,n)^{16}$O Cross Section with Implications for NeutrinoMixing and

Geoneutrino Measurements, Phys. Rev. Lett. **125**, 062501 (2020).

[6] M. Heil, R. Detwiler, R. E. Azuma, A. Couture, J. Daly, J. Goerres, F. Kappeler, R. Reifarth, P. Tischhauser, C. Ugalde, and M. Wiescher, The ^{13}C(α, n) reaction and its role as a neutron source for the s process, Phys. Rev. C **78**, 025803 (2008).

[7] G. Giorginis, V. Khryachkov, V. Corcalciuc, and M. Kievets, The cross section of the ^{16}O$(n, \alpha)^{13}$C reaction in the MeV energy range, Int. Conf. Nucl. Data Sci. Technol. **2007**, 525 (2008).

[8] V. A. Khryachkov, I. P. Bondarenko, B. D. Kuzminov, N. N. Semenova, A. I. Sergachev, and T. A. Ivanova, Giorginis G., (n,α) reactions cross section research at IPPE, EPJ Web Conf. **21**, 03005 (2012).

[9] E. A. Davis, T. W. Bonner, D. W. Worley, and R. Bass, Disintegration of ^{16}O and ^{12}C by fast neutrons, Nucl. Phys. **48**, 169 (1963).

[10] D. Dandy, J. L. Walking, and C. J. Parnell, The cross section for the ^{16}O(n, α) reaction for neutron energies in the range 7 To 12 MeV, A.W.R.E. Aldermaston Reports No.60/68 (1968).

[11] K. K. Sekharan, A. S. Divatia, M. K. Mehta, S. S. Kerekatte, and K. B. Nambiar, O-16(n,α)C-13 cross-sections from the C-13(α,n)O-16 reaction, Phys. Rev. **156**, 1187 (1967).

[12] A. D. Robb, W. A. Schier, and E. Sheldon, Spin and parity assignments for ^{17}O levels from the ^{13}C$(\alpha, n)^{16}$O$_{g.s.}$ reaction, Nucl. Phys. A **147**, 423 (1970).

[13] J. K. Bair and F. X. Haas, Total neutron yield from the reactions ^{13}C$(\alpha, n)^{16}$O and ^{17,18}O$(\alpha$, n$)^{20,21}$Ne, Phys. Rev. C **7**, 1356 (1973).

[14] M. T. Pigni and S. Croft, Consistency of ^{16}O(n, α) cross sections, Phys. Rev. C **102**, 014618 (2020).

[15] A. Plompen, "The status of data for ^{16}O and the program of work for CIELO", talk presented at a workshop of the Collaborative International Evaluated Library Organization (NEMEA-7) (2013), https://www.oecd-nea.org/download/wpec/nemea7/docs/presentations/04_S2_Plompen.pdf.

[16] G. M. Hale and M. W. Paris, "Status and plans for ^{1}H and ^{16}O evaluations by R-matrix analyses of the NN and ^{17}O systems," Talk presented at A workshop of the Collaborative International Evaluated Library Organization (NEMEA-7) (2013), https://www.oecd-nea.org/download/wpec/nemea7/docs/presentations/03_S2_Hale.pdf.

[17] S. Kunieda, T. Kawano, M. Paris, G. Hale, K. Shibata, and T. Fukahori, R-matrix Analysis for n+^{16}O Crosssections up to En = 6.0 MeV with covariances, Nucl. Data Sheets **118**, 250 (2014).

[18] G. M. Hale and M. W. Paris, Neutron cross sections for carbon and oxygen from new R-matrix analyses of the ^{13,14}C and ^{17}O systems, EPJ Web Conf. **146**, 02027 (2017).

[19] D. A. Brown, M. B. Chadwick, R. Capote, A. C. Kahler *et al.*, ENDF/B-VIII.0: The 8*th* Major release of the nuclear reaction data library with CIELO-project cross sections, new standards and thermal scattering data, Nucl. Data Sheets **148**, 1 (2018).

[20] S. Kunieda *et al.*, Overview of JENDL-4.0/HE and benchmark calculation, in *Proceedings of the 2015 Symposium on Nuclear Data, November 19-20, 2015*, Ibaraki Quantum Beam Research Center, Tokai-mura, Ibaraki, Japan (JAEA-Conf 2016-004), 41 (2016), https://jopss.jaea.go.jp/pdfdata/JAEA-Conf-2016-004.pdf.

[21] H. Y. Lee, S. Mosby, R. C. Haight, and M. C. White, ^{16}O(n, α) cross section investigation using LENZ instrument at LANSCE, EPJ Web Conf. **122**, 05004 (2016).

[22] A. F. Gurbich and M. V. Bokhovko, Calibration of 3 MV Tandetron™ accelerator over nominal energy range, Nucl. Instrum. Methods Phys. Res., Sect. B **459**, 81 (2019).

[23] *Handbook of Modern Ion Beam Materials Analysis*, edited by Y. Wang and M. Nastasi (MRS, Warrendale, 2009), Chap. 6, pp. 125–143.

[24] J. L. Colaux, T. Thome, and G. Terwagne, Cross section measurements of the reactions induced by deuteron particles on ^{13}C, Nucl. Instrum. Methods Phys. Res., Sect. B **254**, 25 (2007).

[25] A. F. Gurbich, SigmaCalc recent development and present status of the evaluated cross-sections for IBA, Nucl. Instrum. Methods Phys. Res., Sect. B **371**, 27 (2016).

[26] M. Mayer, Improved physics in SIMNRA 7, Nucl. Instrum. Methods Phys. Res., Sect. B **332**, 176 (2014).

[27] G. W. Kerr, J. M. Morris, and J. R. Risser, Energy levels of ^{17}O from ^{13}C$(\alpha, \alpha_0)^{13}$C and ^{13}C$(\alpha, n)^{16}$O, Nucl. Phys. A. **110**, 637 (1968).

[28] P. S. Prusachenko, T. L. Bobrovsky, I.P. Bondarenko, A. F. Gurbich, V. V. Ketlerov, T. A. Khromyleva, V. A. Khryachkov, V. J. Poryvaev, and U. A. Kobets, The time shift between the neutron and γ-ray timestamps in organic stilbene scintillator, Nucl. Instrum. Methods Phys. Res., Sect. A **1002**, 165296 (2021).

[29] N. V. Kornilov, V. A. Khriatchkov, M. Dunaev, A. B. Kagalenko, N. N. Semenova, V. G. Demenkov, and A. J. M. Plompen, Neutron spectroscopy with fast waveform digitizer, Nucl. Instrum. Methods Phys. Res., Sect. A **497**, 467 (2003).

[30] P. S. Prusachenko, V. A. Khryachkov, V. V. Ketlerov, M. V. Bokhovko, and I. P. Bondarenko, Optimization of the n/γ separation algorithm for a digital neutron spectrometer, Nucl. Instrum. Methods Phys. Res., Sect. A **905**, 160 (2018).

[31] S. Agostinelli *et al.* (GEANT4 Collaboration), Geant4—a simulation toolkit, Nucl. Instrum. Methods Phys. Res., Sect. A **506**, 250 (2003).

[32] J. Allison *et al.* (GEANT4 Collaboration), Recent developments in Geant4, Nucl. Instrum. Methods Phys. Res., Sect. A **835**, 186 (2016).

[33] A. R. Garcia, E. Mendoza, D. Cano-Ott, R. Nolte, T. Martinez, A. Algora, J. L. Tain, K. Banerjee, and C. Bhattacharya, New physics model in GEANT4 for the simulation of neutron interactions with organic scintillation detectors, Nucl. Instrum. Methods Phys. Res.,Sect. A **868**, 73 (2017).

[34] C. Budtz-Jorgensen, H.-H. Knitter, and G. Bortels, Assaying of targets for nuclear measurements with a gridded ionization chamber, Nucl. Instrum. Methods Phys. Res., Sect. A **236**, 630 (1985).

[35] M. Drosg and O. Schwerer, Production of monoenergetic neutrons between 0.1 and 23 MeV: Neutron energies and cross sections, in *Handbook on Nuclear Activation Data*, edited by K. Okamoto (IAEA, Vienna, 1987), Part 1, Chap. 3, pp. 83–161.

[36] M. Drosg and N. Otsuka, Evaluation of the absolute angle-dependent differential neutron production cross sections by the reactions ^{3}H(p, n)^{3}He, ^{1}H(t, n)^{3}He, ^{2}H(d, n)^{3}He, ^{3}H(d, n)^{4}He, and ^{2}H(t, n)^{4}He and of the cross sections of their time-reversed counterparts up to 30 MeV and beyond, Report of International Nuclear Data Center (INDC(AUS)-0019) (2015), https://www-nds.iaea.org/publications/indc/indc-aus-0019.pdf.

[37] M. Drosg, DROSG-2000 neutron source reactions, Documentation Series of the IAEA Nuclear Data Section, IAEA-NDS-87 Rev. 9, (2000), https://www-nds.iaea.org/publications/iaea-nds/iaea-nds-0087rev9.pdf.

[38] See Supplemental Material at http://link.aps.org/supplemental/10.1103/PhysRevC.105.024612 for the numerical values of total and differential cross sections for and reactions.

[39] B. K. Barnes, T. A. Belote, and J. R. Risser, Level assignments in ^{17}O from ^{13}C$(\alpha,\alpha)^{13}$C and ^{13}C$(\alpha,\mathrm{n})^{16}$O, Phys. Rev. **140**, B616 (1965).